

# Three Dimensional Finite-Difference Seismic Signal Propagation

**Mark Moran<sup>+</sup>, Steve Ketcham<sup>+</sup>, Roy Greenfield**

August 1999

<sup>+</sup> USA CRREL

72 Lyme Rd, Hanover NH 03755-1290

603-646-4274

[mmoran@crrel.usace.army.mil](mailto:mmoran@crrel.usace.army.mil)

\* Dept. Geosciences, Penn State University

504 Deike Building

University Park, PA 16802

814-865-5723

[roy@geosc.psu.edu](mailto:roy@geosc.psu.edu)

## Abstract

Moving tracked vehicles excite large-amplitude seismic surface waves that can be used to track and identify them at ranges over 1 km. Furthermore, these surface waves generally possess robust spatial coherence, show a smooth amplitude decay as a function of vehicle range, and are minimally affected by severe meteorological conditions. Because of these properties, seismic signals should be used to augment acoustic sensing in battlefield systems. However, large changes in vehicle signature characteristics can be produced by geological variations. The heightened interest in using seismic signals for battlefield applications has created a need to understand the complex effects produced by the ground on propagating seismic surface waves. High fidelity forward modeling can be used to both explain these effects and to provide raw data for system development. Using synthetic data in this manner can reduce system development time and overall costs, while simultaneously improving system performance.

Geologic inhomogeneity and material properties affect signal characteristics at target ranges as short as 100 m; signals from more distant target ranges are affected to an even greater extent. Horizontal inhomogeneities resulting from subsurface variation and topography, in particular, affect seismic surface wave characteristics. The need to accommodate strong near-surface inhomogeneity and seismic body-wave conversions at geologic boundaries compels the use of discrete numerical propagation approaches. A finite difference time domain (FD-TD) approach was selected as the propagation method for simulating seismic signatures because of the wide availability of sophisticated FD-TD codes and their complete consideration of all 3D body and surface wave energy transfer processes.

We discuss the mathematical basis of our FD-TD code and present simulated propagation results from a large parallel 3D FD-TD elastic model. For portability reasons, the code is written in standard Fortran77 and is parallelized using the Message Passing Interface (MPI) subroutine library. The code has been successfully run on Sun workstation clusters and on massively parallel Cray and IBM platforms. Simulations are discussed for a plane layered geology and for a geology with dominant 3D features. Both results use an explosive pressure impulse placed just under the earth's surface. The 3D geologic model contains an isolated hard rock topographic feature protruding through a layered near-surface soil. In both cases complex seismic waves are observed. In the case of the protruding topographic feature, the results show strong surface wave reflection and refraction around it. These phenomena dramatically affect the character of seismic signals by altering the waveform, by reducing the signal amplitude, and by reducing the spatial coherence of the wavefields. Signal effects of this magnitude would severely impact system performance. Conversely, foreknowledge of these effects can be used advantageously to optimally place autonomous battlefield monitoring systems.

## 1.0 Introduction

Use of synthetic (modeled) data can substantially reduce the time and costs of developing a combat system, while simultaneously improving its reliability. This is achieved by considering how the system will perform

## REPORT DOCUMENTATION PAGE

<b>1. REPORT DATE (DD-MM-YYYY)</b> 01-08-1999	<b>2. REPORT TYPE</b>	<b>3. DATES COVERED (FROM - TO)</b> xx-xx-1999 to xx-xx-1999
<b>4. TITLE AND SUBTITLE</b> Three Dimensional Finite-Difference Seismic Signal Propagation  Unclassified	<b>5a. CONTRACT NUMBER</b>	
	<b>5b. GRANT NUMBER</b>	
	<b>5c. PROGRAM ELEMENT NUMBER</b>	
<b>6. AUTHOR(S)</b> Moran, Mark ; Ketcham, Steve ; Greenfield, Roy ;	<b>5d. PROJECT NUMBER</b>	
	<b>5e. TASK NUMBER</b>	
	<b>5f. WORK UNIT NUMBER</b>	
<b>7. PERFORMING ORGANIZATION NAME AND ADDRESS</b> USA CRREL 72 Lyme Rd  Hanover , NH 03755-1290	<b>8. PERFORMING ORGANIZATION REPORT NUMBER</b>	
<b>9. SPONSORING/MONITORING AGENCY NAME AND ADDRESS</b>  ,	<b>10. SPONSOR/MONITOR'S ACRONYM(S)</b>	
	<b>11. SPONSOR/MONITOR'S REPORT NUMBER(S)</b>	
<b>12. DISTRIBUTION/AVAILABILITY STATEMENT</b> A PUBLIC RELEASE  ,		

**13. SUPPLEMENTARY NOTES****14. ABSTRACT**

Moving tracked vehicles excite large-amplitude seismic surface waves that can be used to track and identify them at ranges over 1 km. Furthermore, these surface waves generally possess robust spatial coherence, show a smooth amplitude decay as a function vehicle range, and are minimally affected by severe meteorological conditions. Because of these properties, seismic signals should be used to augment acoustic sensing in battlefield systems. However, large changes in vehicle signature characteristics can be produced by geological variations. The heightened interest in using seismic signals for battlefield applications has created a need to understand the complex effects produced by the ground on propagating seismic surface waves. High fidelity forward modeling can be used to both explain these effects and to provide raw data for system development. Using synthetic data in this manner can reduce system development time and overall costs, while simultaneously improving system performance.

**15. SUBJECT TERMS**

<b>16. SECURITY CLASSIFICATION OF:</b>			<b>17. LIMITATION OF ABSTRACT</b>	<b>18. NUMBER OF PAGES</b>	<b>19a. NAME OF RESPONSIBLE PERSON</b>
<b>a. REPORT</b> Unclassified	<b>b. ABSTRACT</b> Unclassified	<b>c. THIS PAGE</b> Unclassified	Public Release	12	Fenster, Lynn lfenster@dtic.mil
					<b>19b. TELEPHONE NUMBER</b> International Area Code  Area Code Telephone Number 703 767-9007 DSN 427-9007

under diverse deployment scenarios and by discovering physical processes that exhibit robust environmentally invariant signal characteristics that are specific to a target class.

The central long term objective of our project is to produce high fidelity seismic signatures generated by heavy ground vehicles, such as armor, motorized artillery, or TEL transports, operating in complex geologic settings such as that shown in Figure 1. The approach must be flexible enough to accommodate a wide variety of vehicles, background noise, and geologic settings. Simulations should also consider target ranges of approximately 1 km or more. Greenfield and Moran (1999), Moran et al. (1997, 1998), and Prado (1998) have shown that the seismic signatures of tracked ground vehicles are dominated by surface waves that often contain multiple modal arrivals. Furthermore, the target vehicles of interest are spatially large in extent (relative to a wavelength) and in general they apply both vertical and horizontal tractional and pressure forces to the earth or road surface.

Generating a synthetic seismic signature requires specification of: 1) vehicle forcing functions on the earth, 2) definition of the local geology, and 3) propagation of seismic energy away from the vicinity of the target to a monitoring sensor. Each of these major simulation components presents substantial technical challenges. In this paper, we report on a FD-TD method of seismic energy propagation.

Elastic materials readily support multiple seismic wave types, including compressional (P) and shear (S) body waves, as well as a variety of modal surface wave phases. The latter typically are strongly dispersed. Geologic material properties dramatically affect signal characteristics at target ranges as short as 100 m; signals from more distant target ranges are affected to an even greater extent. Horizontal and vertical geologic inhomogeneities resulting from depositional layering and topography affect seismic surface wave characteristics by creating lossy waveguides, by scattering signals, and through conversions of incident wave phases. The need to accommodate 3D geological inhomogeneity and complex wave conversions compels the use of a discrete numerical propagation approach. A variety of numerical methods have been reported in the geophysical literature. These include wavenumber integration (only applicable for plane layered geologies), finite element (FE), boundary element (BEM), and FD-TD techniques. The wide availability of expertise and the comparative sophistication and maturity of FD-TD codes make this approach the most attractive numerical solution method for our problem.

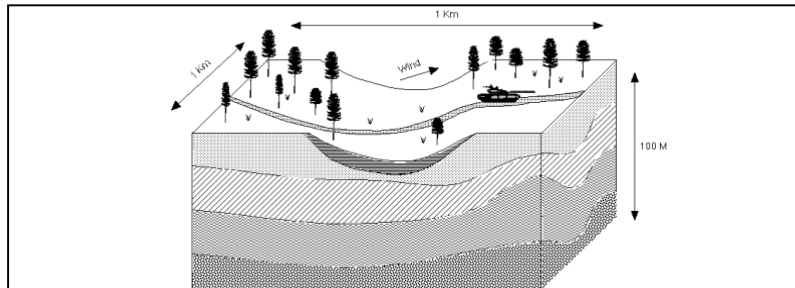


Figure 1. A moving armored vehicle generates large-amplitude seismic signals. Complex geology has a strong effect on signal characteristics. This study applies 3D FD-TD propagation to consider the dynamic source characteristics, complex geology, and spatially distributed noise fields.

## 2.0 Solution Method

We provide a brief summary of the theoretical and numerical methods employed to solve the propagation problem. Greater detail can be found in Hestholm and Ruud (1998). We implement a 3D FD-TD elastic wave equation model using a staggered grid, central difference scheme. Propagating fields are expressed with a velocity-stress parameterization. The differential operator expansions are 8<sup>th</sup> order accurate in space and 2<sup>nd</sup> order accurate in time. A curvilinear coordinate system is used to incorporate the effects of surface topography on seismic energy transfer processes. On the surface of the earth (called the free surface), we impose a zero stress boundary condition. The remaining grid boundaries are terminated using an exponential decay condition.

## 2.1 Equations of Motion

To consider the effects of topography, we incorporate Hestholm and Ruud's (1998) curvilinear coordinate system transformation. The approach begins by specifying the surface of the earth as an arbitrary single-valued elevation function  $z_o(x, y)$ . Consider a curved system with spatial coordinates given by  $\xi$ ,  $\tau$ , and  $\eta$ . The transformation is defined as

$$\xi = x, \quad 1.$$

$$\tau = y, \quad 2.$$

$$\eta = \frac{z}{z_{Max}} z_o(x, y), \quad 3.$$

where  $\eta$  is the depth in the curved coordinate system,  $z$  is the depth below the surface in the rectangular system, and  $z_{Max}$  is the maximum depth of interest. The transform is illustrated in Figure 2. It effectively stretches or shortens the vertical coordinate ( $\eta$ ) corresponding to the variation in  $z_o$ . Using  $\Psi(\xi, \tau, \eta)$  to represent a continuous wave field in the curved coordinate system, we apply equations 1–3 with the chain rule, which leads to

$$\frac{\partial \Psi}{\partial \xi} = \frac{\partial \Psi}{\partial x} + \frac{\partial \Psi}{\partial z} \frac{\partial z}{\partial \xi}, \quad 4.$$

$$\frac{\partial \Psi}{\partial \tau} = \frac{\partial \Psi}{\partial y} + \frac{\partial \Psi}{\partial z} \frac{\partial z}{\partial \tau}, \quad 5.$$

$$\frac{\partial \Psi}{\partial \eta} = \frac{\partial \Psi}{\partial z} + \frac{\partial \Psi}{\partial z} \frac{\partial z}{\partial \eta}. \quad 6.$$

Using 1–3 we define,

$$\frac{\partial z}{\partial \xi} = -\frac{z}{z_o} \frac{\partial z_o}{\partial x} = A, \quad 7.$$

$$\frac{\partial z}{\partial \tau} = -\frac{z}{z_o} \frac{\partial z_o}{\partial y} = B, \quad 8.$$

$$\frac{\partial \eta}{\partial z} = \frac{z_{Max}}{z_o} = C. \quad 9.$$

Applying equations 1–9 to the 3D inhomogeneous elastic wave equation leads to the following particle velocity expressions

$$\rho \frac{\partial u(\xi, \tau, \eta)}{\partial t} = \left[ \frac{\partial \sigma_{\xi\xi}}{\partial x} + A \frac{\partial \sigma_{\xi\xi}}{\partial z} + \frac{\partial \sigma_{\xi\tau}}{\partial y} + B \frac{\partial \sigma_{\xi\tau}}{\partial z} + C \frac{\partial \sigma_{\xi\eta}}{\partial z} + f_{\xi} \right], \quad 10.$$

$$\rho \frac{\partial v(\xi, \tau, \eta)}{\partial t} = \left[ \frac{\partial \sigma_{\xi\tau}}{\partial x} + A \frac{\partial \sigma_{\xi\tau}}{\partial z} + \frac{\partial \sigma_{\tau\tau}}{\partial y} + B \frac{\partial \sigma_{\tau\tau}}{\partial z} + C \frac{\partial \sigma_{\tau\eta}}{\partial z} + f_{\tau} \right], \quad 11.$$

$$\rho \frac{\partial w(\xi, \tau, \eta)}{\partial t} = \left[ \frac{\partial \sigma_{\xi\eta}}{\partial x} + A \frac{\partial \sigma_{\xi\eta}}{\partial z} + \frac{\partial \sigma_{\eta\eta}}{\partial y} + B \frac{\partial \sigma_{\eta\eta}}{\partial z} + C \frac{\partial \sigma_{\eta\eta}}{\partial z} + f_\eta \right], \quad 12.$$

where  $u$ ,  $v$ , and  $w$ , are the vector particle velocities,  $\rho$  is the material density,  $f_i$  are body forces, and  $\sigma_{ij}$  are the stress fields. For isotropic propagation, the 3-by-3 stress matrix is symmetrical around the diagonal and has only 6 unique components. These are

$$\frac{\partial \sigma_{\xi\xi}}{\partial t} = b\lambda + 2\mu \left[ \frac{\partial u}{\partial x} + A \frac{\partial u}{\partial z} + \lambda \frac{\partial v}{\partial y} + B \frac{\partial v}{\partial z} + C \frac{\partial w}{\partial z} \right], \quad 13.$$

$$\frac{\partial \sigma_{\tau\tau}}{\partial t} = b\lambda + 2\mu \left[ \frac{\partial v}{\partial y} + B \frac{\partial v}{\partial z} + \lambda \frac{\partial u}{\partial x} + A \frac{\partial u}{\partial z} + C \frac{\partial w}{\partial z} \right], \quad 14.$$

$$\frac{\partial \sigma_{\eta\eta}}{\partial t} = b\lambda + 2\mu \left[ C \frac{\partial w}{\partial z} + \lambda \frac{\partial u}{\partial x} + A \frac{\partial u}{\partial z} + \frac{\partial v}{\partial y} + B \frac{\partial v}{\partial z} \right], \quad 15.$$

$$\frac{\partial \sigma_{\xi\tau}}{\partial t} = \mu \left[ \frac{\partial v}{\partial x} + A \frac{\partial v}{\partial z} + \frac{\partial u}{\partial y} + B \frac{\partial u}{\partial z} \right], \quad 16.$$

$$\frac{\partial \sigma_{\xi\eta}}{\partial t} = \mu \left[ \frac{\partial w}{\partial x} + A \frac{\partial w}{\partial z} + C \frac{\partial u}{\partial z} \right], \quad 17.$$

$$\frac{\partial \sigma_{\tau\eta}}{\partial t} = \mu \left[ \frac{\partial w}{\partial y} + B \frac{\partial w}{\partial z} + C \frac{\partial v}{\partial z} \right], \quad 18.$$

where  $\mu$  is the shear modulus and  $\lambda$ , Lame's constant. Equations 10 – 18 completely specify all seismic wave phases (compressional, shear, and surface waves) for an isotropic, purely elastic system. The equations of motion given above do not consider energy loss through friction, or visco-elastic response. For propagation in soils, these are important effects that will be included in later investigations through further generalization of equations 10 – 18.

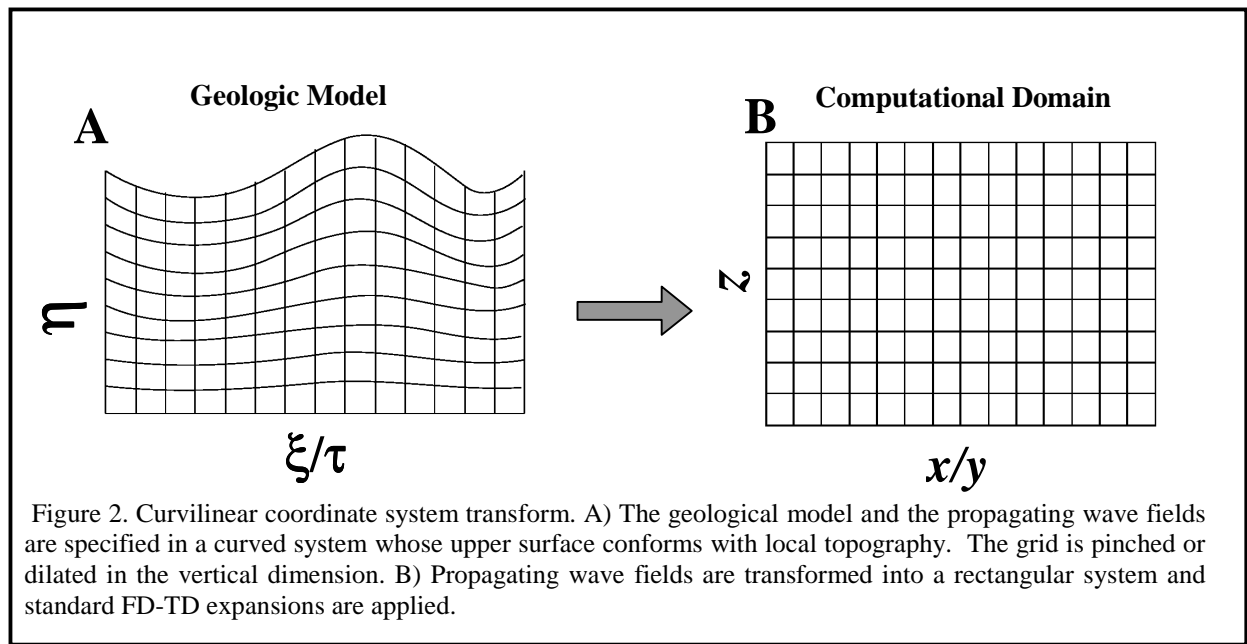


Figure 2. Curvilinear coordinate system transform. A) The geological model and the propagating wave fields are specified in a curved system whose upper surface conforms with local topography. The grid is pinched or dilated in the vertical dimension. B) Propagating wave fields are transformed into a rectangular system and standard FD-TD expansions are applied.

In addition to the traditional time stability criteria requirements (Lines et al., 1999) of FD-TD methods, the curvilinear coordinate basis of this solution approach imposes a spatial stability requirement. It can be readily seen in equations 10 – 18 that if the constants  $A$ ,  $B$ , and  $C$  are larger than 1, as time progresses, the solutions will show roughly geometric growth. To ensure stability, the slopes of the bounding topographic surface should be small relative to the thickness of the model space. This condition is met when

$$\frac{z_o(x, y)}{z_{Max}} = \max \left| \frac{\partial z_0}{\partial x} \right|, \quad 19.$$

$$\left| \frac{\partial z_0}{\partial y} \right| \quad \text{R} \quad 1$$

The Lame material property parameters are related to the compressional (P) and shear (S) body wave propagation speeds ( $V$ ) by

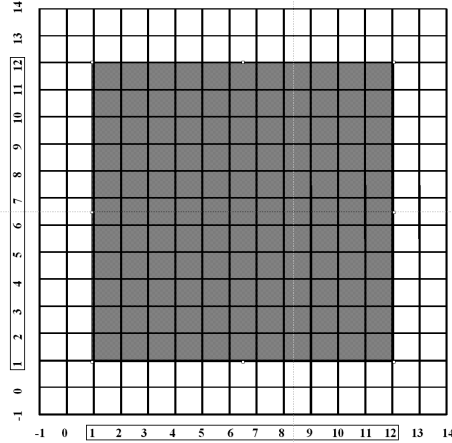
$$V_p = \sqrt{\frac{\lambda + 2\mu}{\rho}}, \quad 20.$$

$$V_s = \sqrt{\frac{\mu}{\rho}}, \quad 21.$$

Density,  $V_p$ , and  $V_s$  are readily observed through direct measurement. Thus, these parameters are used as input to the geologic model.

In our numerical code, the differential operators in equations 10 – 19 are expressed via discrete 8<sup>th</sup> order finite difference expansions in space and 2<sup>nd</sup> order expansions in time. For the purpose of portability, the code is written in Fortran77. FD-TD methods require large computation resources. To make the numerical execution practical, the algorithm has been parallelized using a domain decomposition strategy. This approach apportions the numerical model into a number of computational sub-domains that are associated with a dedicated CPU. As shown in Figure 3, a single processor is usually assigned to each sub-domain. This effectively divides the size of the computation by the number of processors. Exchange of data among processors is accomplished by subroutine calls using the Message Passing Interface (MPI) library. MPI is in the public domain and has become a popular standard for parallel numerical problems. One of its most appealing features is its platform independence. CRREL's parallel code has been successfully run on Sun workstation clusters, and on massively parallel Cray T3E (512 CPU nodes) and IBM SP2 (256 CPU nodes) platforms.

**A) Full Model Domain**



**B) Decomposed Domain**

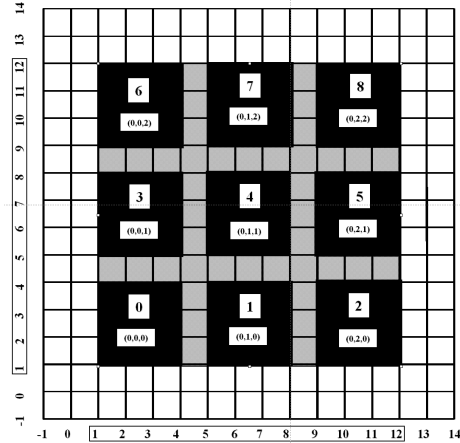


Figure 3. A) A 2D Model on a 12-by-12 rectangular grid. B) The model decomposed into 9 sub-domains. Each sub-domain spans a 4-by-4 grid. Each of these 9 domains is assigned to a single processor that is situated in a 3-by-3 processor mesh topology. MPI provides protocols for exchanging data among processors. In real cases typical models span millions of grid nodes that are decomposed and evaluated on tens of processors.

## 2.2 Boundary Conditions

FD-TD calculations support wave propagation within a bounded region. The bottom and lateral grid terminations are generally not physically real and as a consequence they introduce unwanted reflections. The upper boundary of the computational grid is defined as the earth air interface. This is a naturally occurring termination and is handled by the imposition of free-surface boundary conditions.

In elastic calculations, the surface of the earth represents a comparative vacuum that requires the imposition of special boundary conditions. This is an important aspect of the simulation problem, since the imposition of these special conditions is largely responsible for the occurrence and characteristics of seismic surface waves. Stresses can not be supported in a vacuum. In the curved coordinate system, this requires

$$\frac{\partial u(\xi, \tau, \eta)}{\partial \eta} = -\frac{\partial w(\xi, \tau, \eta)}{\partial \xi}, \quad 22.$$

$$\frac{\partial v(\xi, \tau, \eta)}{\partial \eta} = -\frac{\partial w(\xi, \tau, \eta)}{\partial \tau}, \quad 23.$$

$$\frac{\partial w(\xi, \tau, \eta)}{\partial \eta} = -\frac{\lambda}{\lambda + 2\mu} \left[ \frac{\partial u(\xi, \tau, \eta)}{\partial \xi} + \frac{\partial v(\xi, \tau, \eta)}{\partial \tau} \right]. \quad 24.$$

To apply these stress release conditions, the normal at each surface grid point is calculated from the local topography and the coordinate system transformation is applied. Details of this rotation and transformation are given by Hestholm and Ruud (1998). The result is a system of linear equations, which are solved by direct matrix inversion using 2<sup>nd</sup> order vertical and horizontal particle velocity derivatives from the grid nodes immediately below the free-surface.

Because of practical limitations on computational resources, the spatial extent of the bounded region is often undesirably small. In the confined space, the seismic wavefronts often reflect from the terminated grid with comparatively large amplitudes that do not correspond to reflections observed in the physical world. There are a variety of numerical methods that can be applied to reduce these unwanted boundary reflections. The method implemented here follows Cerjan et al. (1985). In this approach an exponential reduction is applied to the field values inside an annular shell of finite width ( $N\Delta x$ ) whose outer surface is the edge of model domain. The reduction is given by

$$G(n) = e^{-b_{x,n}\Delta x}. \quad 25.$$

Cerjan et al. (1985) recommends  $\alpha=0.015$  and  $N=20$ . For grid positions inside the annular shell, each particle velocity and stress field component is scaled by  $G$  at every time step. The resulting spatial taper is very slight over  $N$ ; however, the reduction occurs at each time step for both the inwardly propagating wave and its returning reflection. We have found that reflections are effectively reduced. However, there is a substantive loss in usable computational volume.

## 3.0 Results

A model run progresses for a user specified number of time steps. At each time step the particle velocity and stress fields are updated at every grid point in the model volume and are thus available as output. Owing to the large amount of data involved, it is frequently desirable to save only a subset of the available volumetric space. In this paper we discuss particle velocity results from vertical or horizontal slices taken from the available 3D model volume at selected times. These are termed snapshots. Corresponding animated results are discussed in the presentation. The relative computational size of the problem can be represented by the total number of grid points in a model volume and the number of time steps in the model run.

Two simulation results are presented. In both cases, a point explosive source is located near the free surface. The first example is for a plane layered geology. The second example uses a geology that contains a small topographic feature, penetrating a shallow low-velocity soil. This geology is common in a number of problematic areas of the world. Both results show complex wave phenomenon that can be exploited for development of system deployment doctrines or in system adaptation. Following these model results, we discuss preliminary validation studies.

### 3.1 Plane Layered Geology

Figure 4 shows two y-z plane snapshots for the vertical component of particle velocity. The model used an 84 x 84 x 84 grid volume with grid separations of 200 m. The center frequency of the excitation source was roughly 10 Hz. In Figure 4A the geologic boundaries are indicated by horizontal dotted lines. Table 1 gives the associated geologic parameters. This model result is representative of a large scale crustal velocity structure. Figure 4A gives an image frame at 0.008 s into the simulation. It shows that the explosive pressure point source has been initiated approximately 0.75 wavelengths below free surface. The apparent dipole pattern is a consequence of only showing the vertical particle motion. Figure 4B shows a snapshot at 1.064 s. A variety of labeled wavefronts are present. The labeled 1 event shows an upwardly propagating primary reflection from L0 – L1 layer boundary, 2 shows the primary transmitted wavefront in layer L2. Note the wavelength elongation in this higher velocity layer. The labeled 3 event shows P-headwaves at earth-air interface and L0-L1 interface. Labeled wavefront 4) shows a downwardly propagating P-S reflection from earth air interface. And barely discernable at label 5 is a slight amplitude reduction on the primary attributable to the onset of the boundary absorption condition.

Layer label	Density (kg/m <sup>3</sup> )	V <sub>p</sub> (m/s)	V <sub>s</sub> (m/s)	Grid Dimension
L0	1500	6000	3400	84 x 84 x 84
L1	2000	7000	4500	
L2	2000	8000	5500	

Table 1. Geologic model parameters used to produce the results shown in Figure 4.

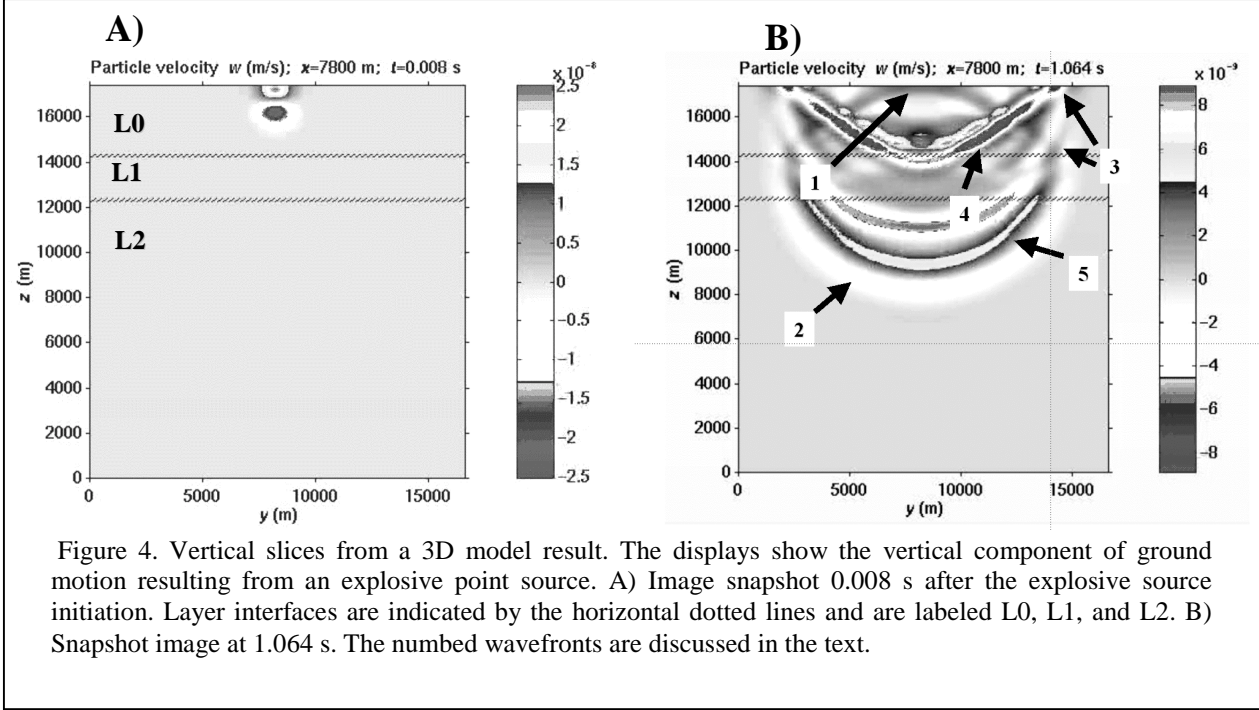


Figure 4. Vertical slices from a 3D model result. The displays show the vertical component of ground motion resulting from an explosive point source. A) Image snapshot 0.008 s after the explosive source initiation. Layer interfaces are indicated by the horizontal dotted lines and are labeled L0, L1, and L2. B) Snapshot image at 1.064 s. The numbered wavefronts are discussed in the text.

### 3.2 Topographic Intrusion

A large percentage of the world's most troubled regions are characterized by mountainous terrain. Familiar examples include North and South Korea, Taiwan, the Balkans, Afghanistan, and northern Iraq. The list is extensive. Independent of all other factors, rugged terrains will have a pronounced effect on acoustic and seismic signal properties. One of the unique features of our simulation approach is the ability to simulate the effects of topography on seismic waves. In Figure 5 we illustrate an idealization of a common geologic situation. The figure shows a rock outcrop penetrating through a 15-m-thick compact soil. The outcrop extends 8 m above the surrounding soil horizon. The constituent geologic parameters are given in Table 2. They are typical of values seen at shallow depths. The explosive source is placed roughly 3 m below the free surface. The source is broadband with a center frequency of roughly 40 Hz. The model extent is 165 x 156 x 62 m and uses a 132 x 120 x 48 node grid. There were 2400 time steps. With an eight processor Sun work station cluster, the runtime was roughly 7.5 hours.

Layer label	Density (kg/m <sup>3</sup> )	V <sub>p</sub> (m/s)	V <sub>s</sub> (m/s)	Grid Dimension
L0	1800	800	461	132x120x48
L1	2400	1800	1040	

Table 2. Geologic model parameters used to produce the results shown in Figure 6.

An animation of the vertical component of particle motion over the free surface and in a cross section was generated in this simulation. Figure 6A shows a snapshot of the free-surface at 0.097 s. In this figure, we see large-amplitude surface waves radiating from the source point. In the vicinity of the topographic feature, we see that faster traveling, lower amplitude P-waves have refracted through the hill. These waves have followed a path of shortest time through the underlying high velocity rock layer. Figure 6B gives a snapshot of the free-surface at roughly 0.2 s. In this time frame, we clearly see that the hill has scattered incident waves with a roughly circular radiation pattern.

On the lateral ( $y$ ) sides of the hill, these scattered waves are interfering with surface waves that are diffracting around the hill. This complex scattering phenomenon will clearly affect sensor performance.

As alluded to in previous sections, and as seen in the above discussion, topography has a pronounced effect on seismic signal properties and will therefore affect the performance of systems that use seismic sensors. To show the utility of simulations in predicting system performance, we use the topographic simulation results to quantify several key signal characteristics that are indicative of tracking performance. In Figure 7A we have plotted the vertical component of ground motion as a function of time for a 60-element line array, on the free-surface, that spans the  $x$  dimension of the model. Time series such as this can be convolved with a WAM or Raptor sensor response function. The resulting data can then be used in WAM or Raptor system simulations in the same way that field data are used. The most striking characteristic of Figure 7A is the large waveform variation across the sensor array. The waveforms seen in the vicinity of the source can be thought of as the “source signature.” In the vicinity of the hill the source signature has been radically altered. In practical terms this implies that target features needed for classification will be obscured. In Figure 7B we show the relative peak-to-peak amplitude variation across the array. Just in front of the hill, at approximately  $x = 70$  m, there is an abrupt 15 dB amplitude reduction over a span of less than 7 m. If a system is placed in this region and it uses signal level to estimate target range, then the target will appear to be over 4 times further away than the actual range. In Figure 7C we plot an average of the mean signal coherence ( $\Gamma$ ) at the source center frequency (40 Hz). In this coherence plot, a moving average is constructed at 5-m intervals using a 20-m-long subarray. High signal coherence is needed for estimating target bearings. In the plot we see that the coherence function is generally very high. However, there is a dramatic drop in coherence in front of the hill. In this region, a system’s bearing estimation accuracy will be severely reduced.

In this scenario, all three major ground sensor system functions will be adversely affected in a small region in front of the hill. An analysis approach such as this can be used to inform the user of where optimal system performance can be achieved for any given geological situation. Furthermore, system developers can use information such as this to select robust signal characteristics for processing and to specify the hardware needed to maintain a desired performance level.

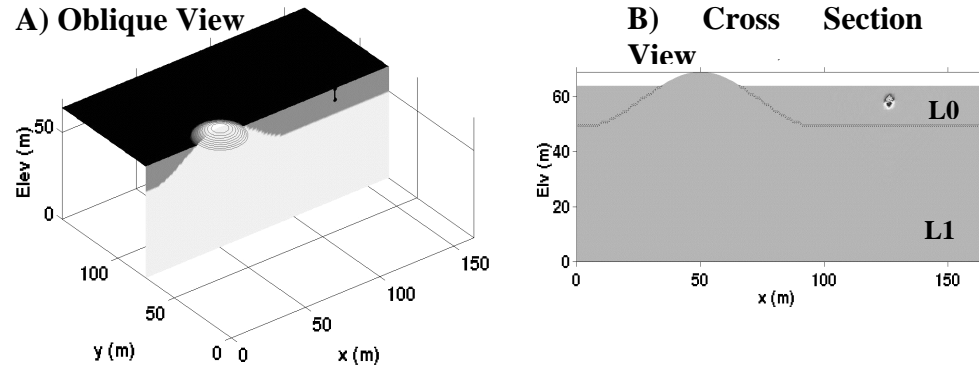


Figure 5. A common geological condition in mountainous zones is a hard-rock intrusion penetrating a shallow low-velocity soil. Model results are obtained for the idealized geology given in this figure. A) and B) show oblique and cross-sectional views of this 3D scenario. Table 2 gives the material properties.

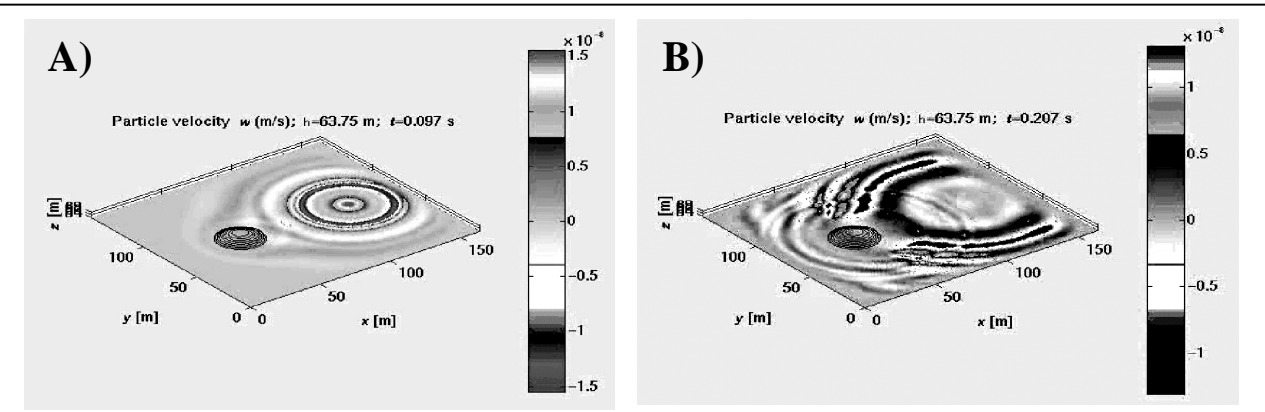


Figure 6. A) Vertical component of ground motion image at 0.097 s. Concentric surface waves are radiating from the surface point directly above the source. Low amplitude P waves have refracted through the hill. B) Image frame at roughly 0.2 s. Strong surface wave diffraction is occurring at the hill. Low-amplitude highly coherent wavefronts are seen moving across the hill.

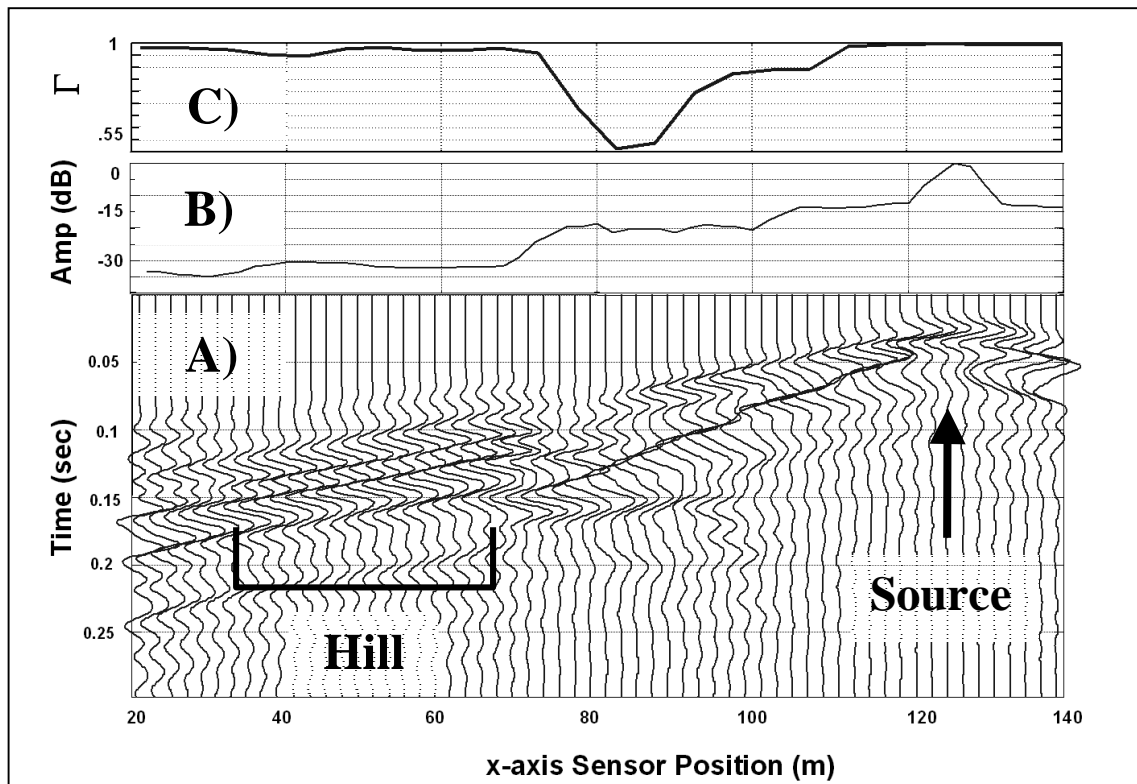


Figure 7. A) Time series of vertical ground motion for a linear array of grid points along the surface. B) Peak-to-peak amplitude variation across the array. In the vicinity of the hill there is an abrupt, 15-dB amplitude reduction in signal levels. C) Mean coherence ( $\Gamma$ ) across the linear array shows a large reduction just in front of the hill.

### 3.3 Preliminary Numerical Propagation Validation

The FD-TD propagation model must accurately represent real physical processes. An extensive field validation is planned in later years of this project. Short of a comparison to field data, preliminary numerical validation can be made by comparing our FD-TD model output to other widely accepted numerical results. In this

discussion, we compare seismograms produced by our program to seismograms produced by the wavenumber integration program OASP. OASP is a component of the Oases package of programs (Version 2.1) (Schmidt, 1997). It uses seismic sources in horizontally layered media. The Oases program has been extensively tested and results from it have been widely reported in the literature.

Our preliminary OASES/FD-TD comparison uses an explosive source in an uniform half-space. The source is placed at a depth of 5 m below the free surface. The geologic parameters used in both models are: P-wave velocity of 700 m/s; S-wave velocity of 400 m/s, and a density of 1800 kg/m<sup>3</sup>. These parameters were used in both the FD-TD and OASP models. The sensor positions are shown in Figure 8A. An overlay of the vertical particle velocity records for the surface sensor positions are shown in Figure 8B. The waveform comparison between the two methods is excellent.

Another check on the FD-TD model results can be made by comparing the P-to-S arrival time curves to ray theory. This is a wave that leaves the source as a P-wave, hits the free surface at an oblique angle, and is partially converted to an S-wave. The comparison can be done by considering a snapshot from the FD-TD model result. In Figure 9A we show a snapshot of the vertical particle velocity at time 0.1 s. The P-to-S surface reflection is the strong linear feature that runs from  $x = 70$  m at the surface to  $x = 30$  m at a depth of 25 m. Figure 9B gives a contour plot of the predicted arrival times for the P-to-S surface reflection based on ray theory. It shows the same P-S linear trend as that observed in Figure 9A. This agreement confirms the correctness of the linear wavefront character, as well as the P-S arrival time.

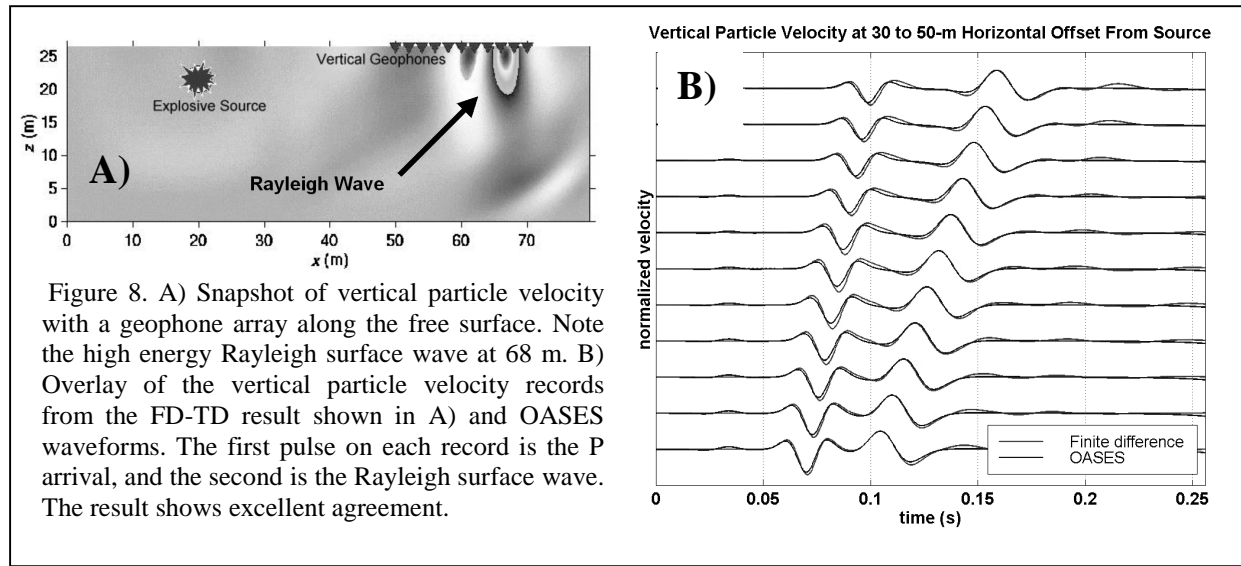


Figure 8. A) Snapshot of vertical particle velocity with a geophone array along the free surface. Note the high energy Rayleigh surface wave at 68 m. B) Overlay of the vertical particle velocity records from the FD-TD result shown in A) and OASES waveforms. The first pulse on each record is the P arrival, and the second is the Rayleigh surface wave. The result shows excellent agreement.

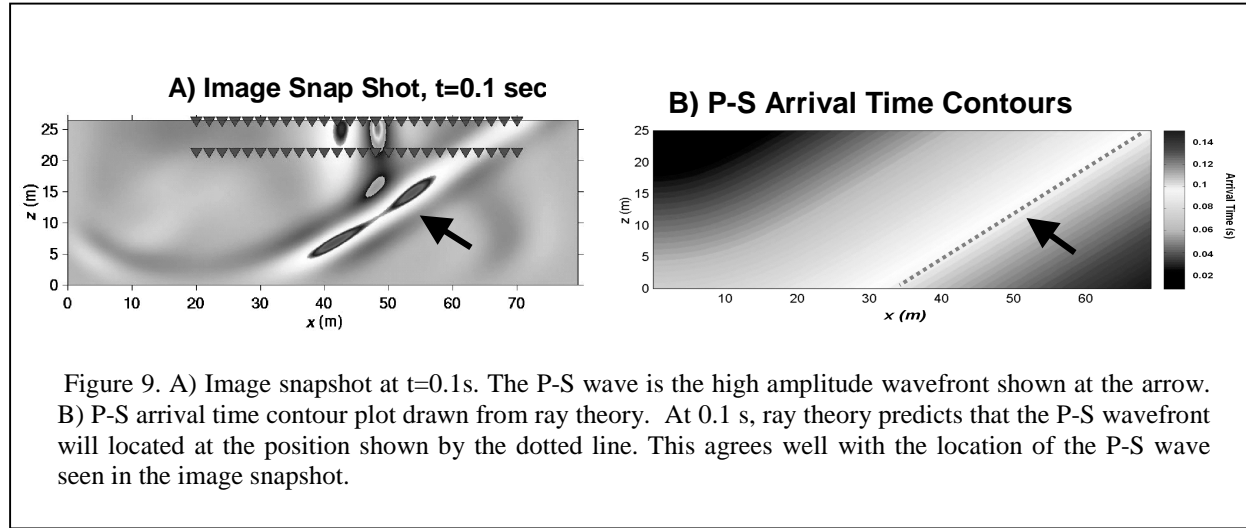


Figure 9. A) Image snapshot at  $t=0.1$  s. The P-S wave is the high amplitude wavefront shown at the arrow. B) P-S arrival time contour plot drawn from ray theory. At 0.1 s, ray theory predicts that the P-S wavefront will located at the position shown by the dotted line. This agrees well with the location of the P-S wave seen in the image snapshot.

## 4.0 Summary

High fidelity simulated data can reduce system development costs and time. In this paper we report on the mathematical basis for a new FD-TD method for simulating propagating seismic signals. The technique uses a curved coordinate system that conforms to the surface topography of the earth. The algorithm has been parallelized following a domain decomposition strategy. For portability it is written in Fortran77 and uses the standard MPI subroutine library to distribute sub-domains across a processor mesh. The code has been successfully run on clusters of workstations and on massively parallel Cray and IBM platforms. A flexible source formulation is implemented that allows pressure and shear force excitations.

Preliminary results are given for a plane layered model and for a rock-outcrop penetrating a layer of soil. Both models show complex seismic propagation phenomena. In the later case, topography is shown to have a pronounced effect on the spatial character of the data. In particular, waveforms are severely altered, amplitudes are reduced by over 15 dB over distances of a few meters, and the spatial coherence of waveforms is reduced from 0.95 to 0.55 over a few meters distance. All three of these characteristics have important implications for ground vehicle tracking performance in battlefield systems that use seismic data.

A preliminary numerical comparison between our FD-TD code and OASIS wavenumber integration models shows excellent waveform and arrival time agreement. Furthermore, the spatial character of P-S wavefronts and the P-S wave arrival times seen in our FD-TD model are in excellent agreement with ray theory predictions.

## Acknowledgements

The authors thank Dr. Stig Hestholm, formerly of Rice University, for providing the basis of the model used in this project. We also express appreciation to Dr. Joyce Nagle for administrative and contract support and Cpt. Tom Gilligan, US Army, for interagency coordination and program development support.

This work was funded by the US Army Office of the Program Manager for Mines, Countermines, and Demolitions, and the US Army Corps of Engineers PE62784/AT42 and PE61102/AT24 work units. Work at Penn State was supported by contract DACA989-98-K-0004.

## References

- Cerjan, C., Kosloff, R. and Reshef, M., 1985, A nonreflecting boundary condition for discrete acoustic-wave and elastic-wave equations: *Geophysics*, vol. 50, 705-708.
- Greenfield, R., and Moran M., 1999, Direction estimation performance using seismic signals from moving vehicles, in preparation for submission to the *Bull. Seis. Soc. Am.*
- Hestholm S., and Ruud, B., 1998, 3-D finite-difference elastic wave modeling including surface topography, *Geophysics*, vol. 63, pp. 613-622.
- Moran, M, and Greenfield, R, 1997, Seismic Detection of Military Operations, 97-CEP-511-1, US Army Maneuver Support Battle Laboratory, Ft. Leonard Wood, MO.
- Moran, M., Boulanger, P., Greenfield, R., and Gilligan, T., 1998, Range Estimation with Seismic Sensors for Early Detection, 98-CEP-0505, US Army Maneuver Support Battle Laboratory, Ft. Leonard Wood, MO.
- Prado, G, 1998, SenTech Inc., Boston, MA, presentation materials and personal communications.
- Lines, L., Slawinski, R., and Bording, R., 1999, A recipe for stability of finite-difference wave-equation computations; *Geophysics*, vol. 64, pp. 967-969
- Schmidt, H., 1997, OASES, Version 2.1 User Guide and Reference Manual, Dept. of Ocean Engineering, MIT, Camb., MA.